

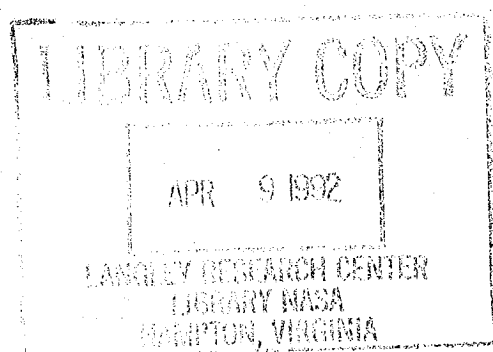
NASA Technical Memorandum 105619

NASA-TM-105619 19920011278

# Implementation/Validation of a Low Reynolds Number Two-Equation Turbulence Model in the Proteus Navier-Stokes Code — Two-Dimensional/Axisymmetric

Trong T. Bui  
*Lewis Research Center*  
*Cleveland, Ohio*

April 1992



**NASA**



# IMPLEMENTATION/VALIDATION OF A LOW REYNOLDS NUMBER TWO-EQUATION TURBULENCE MODEL IN THE PROTEUS NAVIER-STOKES CODE— TWO-DIMENSIONAL/AXISYMMETRIC

Trong T. Bui  
NASA Lewis Research Center  
Cleveland, Ohio

## ABSTRACT

The implementation and validation of the Chien low Reynolds number  $k$ - $\epsilon$  turbulence model in the two-dimensional/axisymmetric version of Proteus, a compressible Navier-Stokes computer code, are presented. The set of  $k$ - $\epsilon$  equations are solved by marching in time using a coupled alternating direction implicit (ADI) solution procedure with generalized first- or second-order time differencing. To validate Proteus and the  $k$ - $\epsilon$  turbulence model, laminar and turbulent computations have been done for several benchmark test cases: incompressible fully developed 2-D channel flow, fully developed axisymmetric pipe flow, boundary layer flow over a flat plate, and turbulent Sajben subsonic/transonic diffuser flows. Proteus results from these test cases showed good agreement with analytical results and experimental data. Detailed comparisons of both mean flow and turbulent quantities demonstrated that the Chien  $k$ - $\epsilon$  turbulence model gives good results over a wider range of turbulent flows than the Baldwin-Lomax turbulence model in the Proteus code with no significant CPU time penalty for more complicated flow cases.

## NOMENCLATURE

$c_f$	Local skin friction coefficient
$H$	Channel halfwidth
$J$	Jacobian matrix of the generalized grid transformation
$k$	Turbulent kinetic energy
$l$	Length
$M_{\max}$	Maximum core Mach number in the Sajben diffuser
$P$	Static pressure
$P_e$	Exit static pressure
$P_k$	Production rate of turbulent kinetic energy
$P_t$	Inlet total pressure
$R$	Pipe radius for axisymmetric pipe flows
$R$	Pressure ratio for Sajben diffuser flows, $P_e/P_t$
$Re_H$	Reynolds number based on channel centerline velocity and halfwidth
$Re_R$	Reynolds number based on pipe centerline velocity and radius
$Re_r$	Reference Reynolds number, $(\rho_r u_r l_r)/\mu_r$
$Re_x$	Reynolds number based on freestream velocity and distance along flat plate
$Re_\theta$	Reynolds number based on freestream velocity and momentum thickness
$T$	Static temperature
$T_t$	Inlet total temperature
$t$	Physical time
$u^+$	Non-dimensional velocity, $u/u_\tau$
$u_\tau$	Shear velocity, $\sqrt{\frac{\tau_w}{\rho}}$
$u, v$	Velocities in the Cartesian $x$ and $y$ directions for 2-D planar equations or in the cylindrical $x$ and $r$ directions for axisymmetric equations
$w$	Velocities in the swirl direction in the axisymmetric equation

$x, r$	Cylindrical axial and radial coordinates
$x, y$	Cartesian coordinates
$y_n$	Minimum distance from the nearest solid wall
$y^+$	Non-dimensional wall coordinates
$\delta$	Boundary layer thickness
$\epsilon$	Dissipation rate of turbulent kinetic energy
$\mu, \mu_t$	Laminar and turbulent viscosity coefficients
$\rho$	Static density
$\tau$	Computational time
$\xi, \eta$	Computational coordinates

## SUBSCRIPTS

$o$	Centerline flow properties
$r$	Dimensional reference conditions

## INTRODUCTION

Two-equation turbulence models are often used in conjunction with Reynolds-averaged Navier-Stokes computer codes to simulate turbulent flow fields, and there has been a considerable amount of research devoted to these models. However, previous turbulence research projects often concentrated on deriving and validating the turbulence models without devoting the considerable amount of efforts required to take a two-equation turbulence model from pure turbulence research to practical engineering calculations. As a result, there is a need to incorporate well proven two-equation turbulence models into a computer code that is user-oriented, well documented, and easy to use. It is hoped that this will permit fluid dynamicists to quickly and efficiently perform CFD calculations involving two-equation turbulence models for a wide variety of turbulent flow fields. In this paper, the implementation and validation of the Chien low Reynolds number  $k$ - $\epsilon$  turbulence model (Chien, 1982) in the two-dimensional/axisymmetric version of Proteus (Towne et al., 1990), a compressible Navier-Stokes computer code, will be described.

## IMPLEMENTATION

Algebraic turbulence models are simple to use and require little computational time. As a result, a popular algebraic turbulence model, the Baldwin-Lomax turbulence model (Baldwin and Lomax, 1978), is available in the Proteus code. However, it has generally been accepted that two-equation turbulence models are more general than algebraic models while still requiring a reasonable amount of computational time. In a review by Patel et al., 1985, the low Reynolds number two-equation models of Launder and Sharma, Chien, Lam and Bremhorst, and Wilcox and Rubesin are found to perform better than the others. For the current implementation, the Chien  $k$ - $\epsilon$  model was chosen for the following reasons:

- Its low-Reynolds number terms are approximated by simple algebraic relations. This reduces the computational time and improves the numerical stability of the  $k$ - $\epsilon$  model in the near wall region.
- Its boundary conditions for  $k$  and  $\epsilon$  at the wall are simple.
- It gives reasonable turbulent and mean flow results near a solid wall.
- It has been used by other researchers in Navier-Stokes calculations with good results (Sahu and Danberg, 1986, Nichols, 1990).

In this implementation, the Proteus philosophy of code readability and modularity has been strictly adhered to. To optimize performance on the Cray computers, the Fortran coding of the Chien

k-ε model has been vectorized as much as possible. Additional logic has been provided to handle flows with multiple solid surfaces and axisymmetric flows with or without swirl.

## CHIEN k-ε TURBULENCE EQUATIONS

The two-dimensional/axisymmetric Chien k-ε equations are transformed into generalized nonorthogonal body-fitted coordinates. For the 2-D case, the following generalized grid transformation is used to transform the k-ε equations from physical (x,y,t) coordinates to computational (ξ,η,τ) coordinates:

$$\xi = \xi(x,y), \quad \eta = \eta(x,y), \quad \text{and} \quad \tau = t \quad (1)$$

The transformed 2-D k-ε equations can be written in vector notation as:

$$\frac{\partial \hat{W}}{\partial \tau} + \frac{\partial \hat{F}}{\partial \xi} + \frac{\partial \hat{G}}{\partial \eta} = \hat{S} + \hat{T} \quad (2)$$

where

$$\hat{W} = \frac{1}{J} \begin{bmatrix} \rho k \\ \rho \varepsilon \end{bmatrix} \quad (3)$$

$$\hat{F} = \hat{F}_c - \hat{F}_d - \hat{F}_m \quad (4)$$

$$\hat{G} = \hat{G}_c - \hat{G}_d - \hat{G}_m \quad (5)$$

$$\hat{S} = \frac{1}{J} \begin{bmatrix} P_k - Re_r \rho \varepsilon \\ C_1 P_k \frac{\varepsilon}{k} - Re_r C_2 \rho \frac{\varepsilon^2}{k} \end{bmatrix} \quad (6)$$

$$\hat{T} = \frac{1}{J} \begin{bmatrix} -\frac{2}{Re_r} \frac{\mu}{y_n^2} k \\ -\frac{2}{Re_r} \frac{\mu \varepsilon}{y_n^2} \end{bmatrix} \quad (7)$$

$$\hat{F}_c = \frac{1}{J} \begin{bmatrix} \xi_x \rho u k + \xi_y \rho v k \\ \xi_x \rho u \varepsilon + \xi_y \rho v \varepsilon \end{bmatrix} \quad (8)$$

$$\hat{F}_d = \frac{1}{J Re_r} \begin{bmatrix} \mu_k (\xi_x^2 + \xi_y^2) k_\xi \\ \mu_\varepsilon (\xi_x^2 + \xi_y^2) \varepsilon_\xi \end{bmatrix} \quad (9)$$

$$\hat{F}_m = \frac{1}{J Re_r} \begin{bmatrix} \mu_k (\xi_x \eta_x + \xi_y \eta_y) k_\eta \\ \mu_\varepsilon (\xi_x \eta_x + \xi_y \eta_y) \varepsilon_\eta \end{bmatrix} \quad (10)$$

$$\hat{G}_c = \frac{1}{J} \begin{bmatrix} \eta_x \rho u k + \eta_y \rho v k \\ \eta_x \rho u \varepsilon + \eta_y \rho v \varepsilon \end{bmatrix} \quad (11)$$

$$\hat{G}_d = \frac{1}{J Re_r} \begin{bmatrix} \mu_k (\eta_x^2 + \eta_y^2) k_\eta \\ \mu_\varepsilon (\eta_x^2 + \eta_y^2) \varepsilon_\eta \end{bmatrix} \quad (12)$$

$$\hat{G}_m = \frac{1}{J Re_r} \begin{bmatrix} \mu_k (\xi_x \eta_x + \xi_y \eta_y) k_\xi \\ \mu_\varepsilon (\xi_x \eta_x + \xi_y \eta_y) \varepsilon_\xi \end{bmatrix} \quad (13)$$

where

$$\mu_k = \mu + \frac{\mu_t}{\sigma_k}, \quad \mu_\varepsilon = \mu + \frac{\mu_t}{\sigma_\varepsilon} \quad (14)$$

$$P_k = \frac{\mu_t}{Re_r} P_l - \frac{2}{3} \rho k P_2 \quad (15)$$

$$P_l = 2 \left[ \left( \frac{\partial u}{\partial x} \right)^2 + \left( \frac{\partial v}{\partial y} \right)^2 \right] - \frac{2}{3} \left[ \frac{\partial u}{\partial x} + \frac{\partial v}{\partial y} \right]^2 + \left[ \frac{\partial u}{\partial y} + \frac{\partial v}{\partial x} \right]^2 \quad (16)$$

$$P_2 = \frac{\partial u}{\partial x} + \frac{\partial v}{\partial y} \quad (17)$$

The turbulent viscosity is given by

$$\mu_t = C_\mu \rho \frac{k^2}{\varepsilon} \quad (18)$$

The empirical constants are the same as those used in the original Chien formulations:

$$\sigma_k = 1.0, \quad \sigma_\varepsilon = 1.3$$

$$C_1 = 1.35, \quad C_2 = 1.8 \left[ 1 - \frac{2}{9} e^{\frac{-R_t^2}{36}} \right]$$

$$C_\mu = 0.09 \left( 1 - e^{-0.0115 y^+} \right), \quad \text{where } R_t = \frac{\rho k^2}{\mu \varepsilon}$$

Note that  $y_n$  is the minimum distance to the nearest solid wall, and  $y^+$  is computed from  $y_n$ . The production of turbulent kinetic energy  $P_k$  includes the full Boussinesq approximation for compressible flows. All of the above equations have been nondimensionalized using appropriate normalizing conditions (Anderson et al., 1984). The turbulent kinetic energy  $k$  has been nondimensionalized by  $u_r^2$ , and turbulent dissipation rate  $\varepsilon$  by  $\rho u_r^4 / \mu_r$ .

Using the transformation of equation (1) with  $y$  replaced by  $r$ , the transformed axisymmetric  $k$ - $\varepsilon$  equations for the Chien model can be written using vector notation as

$$\frac{\partial(r\hat{W})}{\partial\tau} + \frac{\partial(r\hat{F})}{\partial\xi} + \frac{\partial(r\hat{G})}{\partial\eta} = r(\hat{S} + \hat{T}) \quad (19)$$

where  $\hat{W}$ ,  $\hat{F}$ ,  $\hat{G}$ ,  $\hat{S}$ , and  $\hat{T}$  are the same as the corresponding terms in the 2-D transformed equation with the coordinate  $y$  replaced by  $r$ , and

$$P_l = 2 \left[ \left( \frac{\partial u}{\partial x} \right)^2 + \left( \frac{\partial v}{\partial r} \right)^2 + \left( \frac{v}{r} \right)^2 \right] - \frac{2}{3} \left[ \frac{\partial u}{\partial x} + \frac{\partial v}{\partial r} + \frac{v}{r} \right]^2 + \left[ \frac{\partial u}{\partial r} + \frac{\partial v}{\partial x} \right]^2 + \left[ \frac{\partial w}{\partial x} \right]^2 + \left[ r \frac{\partial}{\partial r} \left( \frac{w}{r} \right) \right]^2 \quad (20)$$

$$P_2 = \frac{\partial u}{\partial x} + \frac{\partial v}{\partial r} + \frac{v}{r} \quad (21)$$

In the current implementation, the swirl velocity  $w$  is included in the axisymmetric formulation of the turbulent kinetic energy production term

## SOLUTION ALGORITHM FOR THE $k$ - $\varepsilon$ EQUATIONS

For code modularity in turbulence modeling, the set of  $k$ - $\varepsilon$  equations are lagged in time and solved separately from the Navier-Stokes equations using a finite difference technique. Like the Navier-Stokes equations in Proteus, the  $k$ - $\varepsilon$  equations are solved by marching in time using a coupled alternating direction implicit (ADI) solution procedure with the generalized first- or second-order time differencing scheme of Beam and Warming, 1978. The 2-D  $k$ - $\varepsilon$  equations are solved using the following sequence:

Sweep 1 ( $\xi$  direction)

$$\left\{ I + \frac{\theta_1 \Delta \tau}{1 + \theta_2} \left[ \frac{\partial}{\partial \xi} (A - B) - (M + N) \right] \right\}^n \Delta \hat{W}^* =$$

$$\frac{\theta_1 \Delta \tau}{1 + \theta_2} \left[ \frac{\partial (\Delta \hat{F}_M)}{\partial \xi} + \frac{\partial (\Delta \hat{G}_M)}{\partial \eta} \right]^{n-1} +$$

$$\frac{\Delta \tau}{1 + \theta_2} \left[ -\frac{\partial \hat{F}_C}{\partial \xi} + \frac{\partial \hat{F}_D}{\partial \xi} + \frac{\partial \hat{F}_M}{\partial \xi} - \frac{\partial \hat{G}_C}{\partial \eta} + \frac{\partial \hat{G}_D}{\partial \eta} + \frac{\partial \hat{G}_M}{\partial \eta} + \hat{S} + \hat{T} \right]^n + \frac{\theta_2}{1 + \theta_2} \Delta \hat{W}^{n-1} \quad (22)$$

Sweep 2 ( $\eta$  direction)

$$\left\{ I + \frac{\theta_1 \Delta \tau}{1 + \theta_2} \left[ \frac{\partial}{\partial \eta} (C - D) \right] \right\}^n \Delta \hat{W}^n = \Delta \hat{W}^* \quad (23)$$

Where

$$A = \begin{bmatrix} \xi_x \mu + \xi_y \nu & 0 \\ 0 & \xi_x \mu + \xi_y \nu \end{bmatrix} \quad (24)$$

$$B = \begin{bmatrix} \frac{1}{J Re_r} \mu_k (\xi_x^2 + \xi_y^2) \left( \frac{J}{\rho} \right)_\xi & 0 \\ 0 & \frac{1}{J Re_r} \mu_\epsilon (\xi_x^2 + \xi_y^2) \left( \frac{J}{\rho} \right)_\xi \end{bmatrix} \quad (25)$$

$$C = \begin{bmatrix} \eta_x u + \eta_y v & 0 \\ 0 & \eta_x u + \eta_y v \end{bmatrix} \quad (26)$$

$$D = \begin{bmatrix} \frac{1}{J Re_r} \mu_k (\eta_x^2 + \eta_y^2) \left( \frac{J}{\rho} \right)_\eta & 0 \\ 0 & \frac{1}{J Re_r} \mu_\epsilon (\eta_x^2 + \eta_y^2) \left( \frac{J}{\rho} \right)_\eta \end{bmatrix} \quad (27)$$

$$M = \begin{bmatrix} 2C_\mu \frac{k}{\epsilon} \frac{P_k}{\mu_t} & -C_\mu \frac{k^2}{\epsilon^2} \frac{P_k}{\mu_t} - Re_r \\ C_1 C_\mu \frac{P_k}{\mu_t} + Re_r C_2 \frac{\epsilon^2}{k^2} & -2 Re_r C_2 \frac{\epsilon}{k} \end{bmatrix} \quad (28)$$

$$N = \begin{bmatrix} -\frac{2\mu}{\rho y_n^2 Re_r} & 0 \\ 0 & -\frac{2\mu}{\rho y_n^2 Re_r} e^{\frac{-y^+}{2}} \end{bmatrix} \quad (29)$$

An analogous solution procedure is used for the axisymmetric  $k$ - $\epsilon$  equations. The parameters  $\theta_1$  and  $\theta_2$  determine the type of time differencing scheme used (Beam and Warming, 1978). To approximate spatial partial derivatives, a variable centered formula is used. Following Nichols, 1990, the spatial derivatives for the convective terms  $A$ ,  $C$ ,  $\hat{F}_c$ ,  $\hat{G}_c$  are approximated using first-order upwind

differencing. A first-order backward difference approximation is used for the terms with positive eigenvalues, and a first-order forward difference approximation is used for the terms with negative eigenvalues. Since the k- $\epsilon$  solver uses the same time step as the Navier-Stokes solver, several time step options are available. In addition, the user can specify the number of k- $\epsilon$  iterations per Navier-Stokes iteration and any k- $\epsilon$  time step factor.

The boundary condition types and boundary condition values for k and  $\epsilon$  can be specified at any boundary as a whole or at any point on any boundary. For easy modification and easy evaluation of complicated boundary condition expressions for k and  $\epsilon$ , the boundary conditions are treated explicitly. Spatially periodic boundary conditions for k and  $\epsilon$  are also available and implemented using a periodic block solver. Unlike the Proteus Navier-Stokes solver, artificial viscosities are not used in the k- $\epsilon$  solver. Smoothing is provided by using first-order upwind differencing for the convective terms in the k- $\epsilon$  equations as described above. No artificial bounds or constraints were placed on the computed k and  $\epsilon$  profiles. The only requirement imposed on the k and  $\epsilon$  profiles computed in this implementation is that they both have to be positive.

For computations with the k- $\epsilon$  turbulence model, initial values for k and  $\epsilon$  are required throughout the flow field to start the time marching procedure. The best choice for initial conditions for the k- $\epsilon$  equations will vary from problem to problem, and the user must supply a subroutine that sets up the initial values for k and  $\epsilon$  for the time marching procedure. A default subroutine, subroutine KEINIT, is built into Proteus that computes the initial k and  $\epsilon$  values from an initial or restart mean flow field based on the assumption of local equilibrium (production equals dissipation), and variations of that scheme have been found to be useful in computing the k- $\epsilon$  initial conditions for many turbulent flow calculations.

In subroutine KEINIT, the production rate of turbulent kinetic energy  $P_k$  is first computed from the initial or restart mean flow field using equations (15)-(17), assuming k is zero everywhere. Then the initial profile for the dissipation rate  $\epsilon$  is found using the following relation:

$$\epsilon = \frac{P_k}{Re, \rho} \quad (30)$$

Next, equation (18) is used to compute the initial profile for the turbulent kinetic energy k, and the resulting k and  $\epsilon$  profiles are then used to start the time marching process for the k- $\epsilon$  equations.

## VALIDATION

To validate Proteus and the k- $\epsilon$  model, laminar and turbulent computations have been done for several benchmark test cases: incompressible fully developed 2-D channel flow, fully developed axisymmetric pipe flow, boundary layer flow over a flat plate, and turbulent Sajben transonic diffuser flow. The laminar computations served as confidence checks for the Proteus code as well as test beds for the various combinations of mean flow initial and boundary conditions that would be useful for the turbulent cases.

The turbulent computations were done with both the Baldwin-Lomax and the Chien k- $\epsilon$  turbulence models. The same mean flow boundary conditions were used for laminar and turbulent flow calculations. Unless otherwise stated, the default artificial viscosity and numerical differencing schemes in Proteus were used, initial conditions for the k- $\epsilon$  equations were generated using the subroutine KEINIT mentioned above, and convergence was assumed when the average absolute residual value for each of the mean flow equation became less than  $1 \times 10^{-6}$ . If it was necessary to cluster grid points near a solid wall, the default gridpoint packing option in Proteus was used. This



option uses the Roberts transformation (Roberts, 1971) to pack points near specified boundaries. All of the computations were done on the Cray YMP at NASA-Lewis Research Center.

## FULLY DEVELOPED 2-D CHANNEL FLOW

Figure 1a shows the grid geometry as well as the boundary conditions used for all of the fully developed 2-D channel flow test cases. The plates are separated by a distance  $2H$  in the  $y$  direction and the mean flow is in the  $x$  direction. Because of symmetry, only half of the 2-D channel was modeled.

### Laminar Channel Flow Test Case

Incompressible fully developed laminar flow in a 2-D channel with a centerline Mach number of 0.05 was computed with no turbulence model. For this case,  $Re_H$  is 100. A  $5H \times 1H$  computational domain with  $51 \times 31$  grid points was used. Uniform grid spacing was used in both the streamwise and normal directions. For mean flow initial conditions, the 2-D Poiseuille velocity profile was used. When a CFL number of 20 was used, the converged solution was obtained in 8710 iterations. As can be seen in figure 2a, the agreement between the Proteus result and the exact solution (Daily and Harleman, 1966) is excellent. For a given pressure drop, the centerline velocity computed by Proteus is 1.28% lower than the laminar exact solution, and this difference is observed to increase as the grid becomes coarser or the centerline Mach number is increased. This observation applies to all of the channel flow and pipe flow test cases discussed below. This computation required  $2.20 \times 10^{-5}$  sec/iteration/grid point.

### Turbulent Channel Flow Test Case

The channel flow experiment conducted by Hussein and Reynolds, 1975 was selected for the turbulent fully developed 2-D channel flow test case. Identical flow conditions and grid point distribution were used for both the Baldwin-Lomax and the Chien  $k-\epsilon$  turbulence model.  $Re_H$  used in this case is 32300. A  $5H \times 1H$  computational domain with  $31 \times 61$  grid points was used. Grid points were clustered in the normal direction near the channel wall with approximately 10 grid points located in the viscous sublayer, and the nearest grid point off the wall is at  $y^+ = 0.8$ . Uniform grid spacing was used in the streamwise direction. For mean flow initial conditions, the turbulent velocity profile derived by Musker, 1979 was used. When a CFL number of 40 was used, converged solutions were obtained in 43380 iterations for the Baldwin-Lomax model and 44860 iterations for the Chien  $k-\epsilon$  model. The large number of iterations required for convergence is caused by using a compressible code to compute an incompressible flow.

Results in figures 2b, 2c, and 2e show that the Chien  $k-\epsilon$  model gave better predictions for the internal 2-D channel flow than the Baldwin-Lomax model. In this test case, the centerline velocities computed by Proteus using the Baldwin-Lomax model and the Chien  $k-\epsilon$  model are 0.34% and 3.3% lower than the experimental value, respectively. From figure 2c, it can be seen that the higher centerline velocity computed by the Baldwin-Lomax model is caused by the prominent wake-like behavior of the  $u^+$  profile near the centerline.

In figure 2d, the turbulent kinetic energy profile computed by the Chien  $k-\epsilon$  model is compared with the experimental data from Laufer, 1949 at  $Re_H = 30800$ . The computed outer turbulent kinetic energy profile is slightly higher than the experimental data, but the trend is well predicted. While the near wall data published by Laufer was incomplete, the Chien  $k-\epsilon$  model predicted a prominent peak of turbulent kinetic energy in the near wall region as expected. Figure 2e shows that while the eddy viscosity profile predicted by the Chien  $k-\epsilon$  model gives better agreement with the experimental data than the Baldwin-Lomax model, it is significantly larger than the experimental eddy viscosity profile near the channel center. This discrepancy is also observed by Myong and Kasagi, 1990 in their evaluation of the Launder-Sharma and the Lam-Bremhorst low Reynolds number  $k-\epsilon$  models. The turbulent computations with the Baldwin-Lomax model and the Chien  $k-\epsilon$  model required  $2.36 \times 10^{-5}$  sec/iteration/grid point and  $3.21 \times 10^{-5}$  sec/iteration/grid point, respectively.

## FULLY DEVELOPED AXISYMMETRIC PIPE FLOW

Figure 1b shows the grid geometry as well as the boundary conditions used for all of the fully developed axisymmetric pipe flow test cases. The pipe radius is  $R$ , and the mean flow is in the  $x$  direction. Because of symmetry, only half of the pipe was modeled. Both the Navier-Stokes and the  $k$ - $\epsilon$  solvers were used in axisymmetric mode.

### Laminar Pipe Flow Test Case

Incompressible fully developed laminar flow in an axisymmetric pipe with a centerline Mach number of 0.05 was computed with no turbulence model. For this case,  $Re_R$  is 100. A  $5R \times 1R$  computational domain with  $51 \times 31$  grid points was used. Uniform grid spacing was used in both the axial and radial directions. For mean flow initial conditions, the Poiseuille velocity profile was used. When a CFL number of 20 was used, the converged solution was obtained in 3500 iterations. As can be seen in figure 3a, the agreement between the Proteus result and the exact solution (Daily and Harleman, 1966) is excellent for both the velocity profile and pressure drop. For a given pressure drop, the centerline velocity computed by Proteus is 0.58% lower than the laminar exact solution. This computation required  $2.49 \times 10^{-5}$  sec/iteration/grid point.

### Turbulent Pipe Flow Test Case

The pipe flow experiment conducted by Laufer, 1952 was selected for the fully developed axisymmetric pipe flow test case. Identical flow conditions and grid point distribution were used with both the Baldwin-Lomax and the Chien  $k$ - $\epsilon$  turbulence model. The  $Re_R$  used in this case is 250000. A  $5R \times 1R$  computational domain with  $21 \times 61$  was used. Grid points were clustered in the radial direction near the pipe wall with approximately 8 grid points located in the viscous sublayer, and the nearest grid point off the wall is at  $y^+ = 1.2$ . Uniform grid spacing was used in the axial direction. For  $k$ - $\epsilon$  initial conditions, the default subroutine KEINIT described above was used. When a CFL number of 40 was used, converged solutions was obtained in 17280 iterations for the Baldwin-Lomax model and 13180 iterations for the Chien  $k$ - $\epsilon$  model.

The comparisons in figures 3b-3e show good agreements between experimental and computational results for both the Baldwin-Lomax model and the Chien  $k$ - $\epsilon$  model. As in the turbulent channel flow test case, using the Chien  $k$ - $\epsilon$  model resulted in better mean velocity profiles than the Baldwin-Lomax model (figures 3b-3c). In figure 3d, the turbulent kinetic energy profile computed by the Chien  $k$ - $\epsilon$  model is slightly higher compared with the experimental data from Laufer, 1952, but the peak near the wall and the general trend are well predicted. Figure 3e shows that the Reynolds stress profiles predicted by the Chien  $k$ - $\epsilon$  and the Baldwin-Lomax models agree exactly with the experimental data. In this figure, the Baldwin-Lomax Reynolds stress profile is exactly on top of the Chien  $k$ - $\epsilon$  profile.

In this test case, the centerline velocities computed by Proteus using the Baldwin-Lomax model and the Chien  $k$ - $\epsilon$  model are 2.09% higher and 2.34% lower than the experimental value, respectively. As in the turbulent channel flow test case, the Baldwin-Lomax model predicted a somewhat higher centerline velocity than the Chien  $k$ - $\epsilon$  model. The turbulent computations with the Baldwin-Lomax model and the Chien  $k$ - $\epsilon$  model required  $3.71 \times 10^{-5}$  sec/iteration/grid point and  $4.36 \times 10^{-5}$  sec/iteration/grid point, respectively.

## 2-D BOUNDARY LAYER FLOW

Figure 1c shows the grid geometry as well as the boundary conditions used for all of the 2-D boundary layer test cases. Incompressible laminar and turbulent flows over a flat plate at zero pressure gradient with a freestream Mach number of 0.1 was computed with and without the turbulence models. The mean flow is in the  $x$  direction. For the upstream boundary, the Blasius

velocity profiles were used to specify the  $u$  and  $v$  boundary conditions for both the laminar and turbulent flow cases. To keep approximately the same number of grid points inside the boundary layer at any given  $x$  station, the height of the grid system is increased with the distance downstream of the plate. The grid points are clustered near the solid wall so that, at any given streamwise location, approximately 90 percent of the grid points are located inside the boundary layer. Because of this special grid treatment, the default Proteus grid packing scheme was not used. Instead, an algebraic grid packing scheme described in Hoffmann, 1989 was employed.

### **Laminar Boundary Layer Flow Test Case**

Incompressible laminar boundary layer flow over a flat plate was computed. The computational domain ranges from  $Re_x = 1000$  at the upstream boundary to  $Re_x = 100000$  at the downstream boundary with 51 grid points in the  $x$  direction and 31 grid points in the normal direction. Grid points were clustered in the normal direction near the plate surface. Uniform grid spacing was used in the streamwise direction. For mean flow initial conditions, the Blasius velocity profiles were used. When a CFL number of 20 was used, convergence was reached in 1860 iterations. As can be seen in figures 4a and 4b, the agreement between the Proteus result and the exact solution (Daily and Harleman, 1966) is excellent for both the velocity and local skin friction profiles. This computation required  $2.071 \times 10^{-5}$  sec/iteration/grid point.

### **Turbulent Boundary Layer Flow Test Case**

The incompressible turbulent boundary layer experiment conducted by Klebanoff, 1953 was selected for the turbulent boundary layer flow test case. Identical flow conditions and grid point distribution were used with both the Baldwin-Lomax and the Chien  $k-\epsilon$  turbulence models. The computational domain ranges from  $Re_x = 1.0 \times 10^4$  at the upstream boundary to  $Re_x = 10.0 \times 10^6$  at the downstream boundary with 81 grid points in the  $x$  direction and 51 grid points in the normal direction. Grid points were clustered in the normal direction near the plate surface such that, at  $Re_\theta \approx 7700$ , approximately 10 grid points were located in the viscous sublayer with the nearest grid point off the wall at  $y^+ = 0.5$ . Uniform grid spacing was used in the streamwise direction. In the calculation using the Baldwin-Lomax model, the Blasius velocity profiles were used for the mean flow initial conditions. The CFL values were 5 for the first 300 CPU seconds and 20 thereafter. The converged solution was obtained in 12010 iterations. The computation using the Chien  $k-\epsilon$  model can also be started from the Blasius velocity profiles, but to save Cray CPU time, the Chien  $k-\epsilon$  calculation was started from the converged Baldwin-Lomax solution. The CFL values used in the Chien  $k-\epsilon$  computation were 2 for the first 300 CPU seconds and 10 thereafter. An additional 11920 iterations were required before all of the residual values for each of the mean flow equations leveled out. It should be noted that the number of iterations required for convergence can be significantly reduced if higher freestream Mach numbers were used. For instance, the number of iterations required for convergence was cut in half when the freestream Mach number was increased to 0.3 with virtually no change in the computed results.

Results in figures 4c-4d show that, although there are minor differences between the Baldwin-Lomax and the Chien  $k-\epsilon$  computed velocity profiles, both of those models predicted velocity profiles that are in excellent agreement with the experimental data.

In figure 4e, the turbulent kinetic energy profile computed by the Chien  $k-\epsilon$  model is compared with the experimental data from Klebanoff, 1953. The agreement is very good. In figure 4f, the Chien  $k-\epsilon$  model is seen to give better prediction of the local skin friction coefficient profile than the Baldwin-Lomax model. The flat plate computations with the Baldwin-Lomax model and the Chien  $k-\epsilon$  model required  $1.94 \times 10^{-5}$  sec/iteration/grid point and  $2.73 \times 10^{-5}$  sec/iteration/grid point, respectively.

## SAJBEN TRANSONIC DIFFUSER FLOW

Figure 1d shows the grid geometry as well as the boundary conditions used for all of the Sajben transonic diffuser test cases. Turbulent flow was computed in the converging-diverging duct. The mean flow is in the x direction. Given a fixed inlet total pressure, there can be a strong shock, weak shock, or no shock at all in the diffusing section after the throat, depending on the pressure at the diffuser exit. The weak shock case has been used as a test case in the 2-D Proteus code User's Guide (Towne et al., 1990). In this report, all three cases were computed using both the Baldwin-Lomax model with the Launder-Priddin mixing length formula in the inner region and the Chien k- $\epsilon$  model. A computational domain of 81 grid points in the streamwise direction and 51 grid points in the normal direction was used. To capture the shock in transonic flow cases, more grid points were positioned in the streamwise direction in the diffusing section after the throat. Grid points were also packed in the normal direction near the two solid walls to resolve the viscous regions with the nearest grid point off the wall at  $y^+ \approx 1.5 - 4.0$ . The same grid distribution was used in all three cases. Since second-order time differencing was used in all of the calculations, no residuals were computed. Convergence was assumed when the pressure distributions remained essentially constant for a given fixed pressure drop.

Initially, the Baldwin-Lomax model was used to start the calculation for all three cases. The initial conditions were zero velocity and constant pressure and temperature everywhere in the flow field. For the transonic flow cases, the exit pressure was gradually lowered to  $R = 0.1338$  to establish supersonic flow in the diffusing section after the throat. Then the exit pressure was gradually raised to the appropriate pressure ratio,  $R$  ( $R = 0.72$  for strong shock and  $R = 0.82$  for weak shock) to establish the shock and iterated there using either the Baldwin-Lomax or the Chien k- $\epsilon$  turbulence models. For the subsonic flow case with no shocks, starting from zero initial conditions everywhere, the exit pressure was gradually lowered to  $R = 0.862$  using the Baldwin-Lomax model and then iterated there using either of the turbulence models.

Figures 5a-5f compare the pressure distributions computed by Proteus using the Baldwin-Lomax and the Chien k- $\epsilon$  models with the experimental data used by Hsieh et al., 1987. For the no shock case ( $R = 0.862$ ), the Chien k- $\epsilon$  results agree well with the experimental data while the Baldwin-Lomax model gave pressures that are too low at the throat. Both turbulence models give good results for the weak shock case ( $R = 0.82$ ). For the strong shock case ( $R = 0.72$ ), the Chien k- $\epsilon$  model does a better job of predicting the pressure profile right after the shock. However, both turbulence models predicted pressures that are too high after the shock. This is to be expected, since experimental data published by Hsieh et al., 1987, Bogar et al., 1983 and Salmon et al., 1983 showed that flow separation does occur at the upper wall for the strong shock case, and no special modifications were made to either of the models to compute separated flow. Note that the shock locations for the transonic cases could be fitted better if the grid points were clustered at the shock locations. But since this was a shock capturing analysis, identical grids were used in all cases.

Figures 6a-6f plot the computed Mach number contours for the no shock, weak shock, and strong shock cases, respectively. The Mach contours for the no shock and the weak shock cases computed using the Baldwin-Lomax model look similar to those computed using the Chien k- $\epsilon$  model, but the Baldwin-Lomax model predicted a maximum core Mach number that is too high for both cases. For the strong shock case, the Baldwin-Lomax model incorrectly predicted bottom wall flow separation after the shock, while the Chien k- $\epsilon$  calculation and experimental results showed that separation occurred on the top wall. Using either of the turbulence models, Proteus computed the critical mass flow rate for the transonic diffuser flow cases to be about 1-3% lower than the one-dimensional isentropic equation. For the Sajben diffuser, calculations using the Baldwin-Lomax model and the Chien k- $\epsilon$  model required  $4.00 \times 10^{-5}$  sec/iteration/grid point and  $4.24 \times 10^{-5}$  sec/iteration/grid point, respectively.

## SUMMARY OF VALIDATION CASES

From the above validation cases, one can see that the Chien  $k-\epsilon$  model consistently predicted the correct flow physics for all of the flows under consideration, whereas the Baldwin-Lomax model was having problems with the internal flow cases. The Chien  $k-\epsilon$  model required about 41% more CPU time than the Baldwin-Lomax model for simpler flows such as the flat plate and only about 6% more CPU time for more complicated flows such as the Sajben diffuser. For more complicated flows, especially flows with multiple solid walls, the difference in CPU times required by the Chien  $k-\epsilon$  model and the Baldwin-Lomax model is small. This is because the Baldwin-Lomax model is burdened with repetitious calculations, additional logic, and complicated averaging processes in order to come up with a reasonable turbulent viscosity profile for flows with complex geometries. Whereas in the Chien  $k-\epsilon$  model, more complex flow cases use exactly the same amount of calculations as the simpler flow cases with only changes in boundary conditions.

## CONCLUSIONS

The Chien  $k-\epsilon$  turbulence model has been successfully implemented into the 2-D version of Proteus, a general purpose Navier-Stokes code. Validation test results showed that the Chien  $k-\epsilon$  model gives good results for a wider variety of flows than the Baldwin-Lomax model in Proteus. Also, the above test cases showed that the CPU time required for Proteus calculations using the Chien  $k-\epsilon$  model is only slightly more than the Baldwin-Lomax model for real life flow cases with complicated geometries.

## ACKNOWLEDGEMENTS

The author gratefully acknowledges Simon Chen, Tawit Chitsomboon, Kevin Kirtley, Nan-Suey Liu, Frank Molls, John Schwab, Tsan-Hsing Shih, Ambady Suresh, Charles Towne, and Jeff Yokota for their helpful advice and suggestions at various phases in this project.

## REFERENCES

- Baldwin, B. S., and Lomax, H., "Thin Layer Approximation and Algebraic Model for Separated Turbulent Flows," AIAA Paper 78-257.
- Beam, R. M., and Warming, R. F., "An Implicit Factored Scheme for the Compressible Navier-Stokes Equations," AIAA Journal, Vol. 16, No. 4, April, 1978, pp. 393-402.
- Bogar, T. J., Sajben, M., and Kroutil, J. C., "Characteristic Frequencies of Transonic Diffuser Flow Oscillations," AIAA Journal, Vol. 21, No. 9, September, 1983, pp. 1232-1240.
- Chien, K. Y., "Prediction of Channel and Boundary-Layer Flows with a Low-Reynolds-Number Turbulence Model," AIAA Journal, Vol. 20, No. 1, January 1982, pp. 33-38.
- Coles, D. E., and Hirst, E. A., Editors, *Computation of Turbulent Boundary Layers - 1968*, AFOSR-IFP-Stanford Conference, Vol. II, Stanford University, August 1968.
- Daily, J. W., and Harleman, D. R. F., *Fluid Dynamics*, Addison-Wesley Publishing Company, Inc., Reading, Massachusetts, 1966, pp. 116-200.
- Hoffmann, K. A., *Computational Fluid Dynamics for Engineers*, Engineering Education System, Austin, Texas, 1989, pp. 254.
- Hsieh, T., Wardlaw Jr., A. B., and Collins, P., "Numerical Investigation of Unsteady Inlet Flowfields," AIAA Journal, Vol. 25, No. 1, January 1987, pp. 75-81.
- Hussain, A. K. M. F., and Reynolds W. C., "Measurements in Fully Developed Turbulent Channel Flow," Journal of Fluids Engineering, December 1975, pp. 568-580.
- Klebanoff, P. S., "Characteristics of Turbulence in a Boundary Layer with Zero Pressure Gradient," NACA Report 1247, May 1953.
- Laufer, J., "Investigation of Turbulent Flow in a Two-Dimensional Channel," NACA Report 1053, September 1949.
- Laufer, J., "The Structure of Turbulence in Fully Developed Pipe Flow," NACA Report 1174, October 1952.
- Musker, A. J., "Explicit Expression for the Smooth Wall Velocity Distribution in a Turbulent Boundary Layer," AIAA Journal, Vol. 17, No. 6, June, 1979, pp. 655-657.
- Myong, H. K., and Kasagi, N., "A New Approach to the Improvement of  $k-\epsilon$  Turbulence Model for Wall-Bounded Shear Flow," JSME International Journal, Series II, Vol. 33, No. 1, 1990, pp. 63-72.
- Nichols, R. H., "A Two-Equation Model for Compressible Flows," AIAA Paper 90-0494, 1990.
- Patel, V. C., Rodi, W., and Scheuerer, G., "Turbulence Models for Near-Wall and Low Reynolds Number Flows: A Review," AIAA Journal, Vol. 23, No. 9, September 1985, pp. 1308-1319.
- Roberts, G.O., "Computational Meshes for Boundary Layer Problems," Proceedings of the Second International Conference on Numerical Methods in Fluid Dynamics, *Lecture Notes in Physics*, Vol. 8, Springer-Verlag, New York, 1971, pp. 171-177.

Sahu, J., and Danberg, J. E., "Navier-Stokes Computations of Transonic Flows with a Two-Equation Turbulence Model," AIAA Journal, Vol. 24, No. 11, November 1986, pp. 1744-1751

Salmon, J. T., Bogar, T. J., and Sajben, M., "Laser Doppler Velocimeter Measurements in Unsteady, Separated, Transonic Diffuser Flows," AIAA Journal, Vol. 21, No. 12, December 1983, pp. 1690-1697.

Towne, C. E., Schwab, J. R., Benson, T. J., and Suresh, A., "PROTEUS Two Dimensional Navier-Stokes Computer Code - Version 1.0, Vols. 1-3," NASA TM 102551-102553, March 1990.

## FIGURES

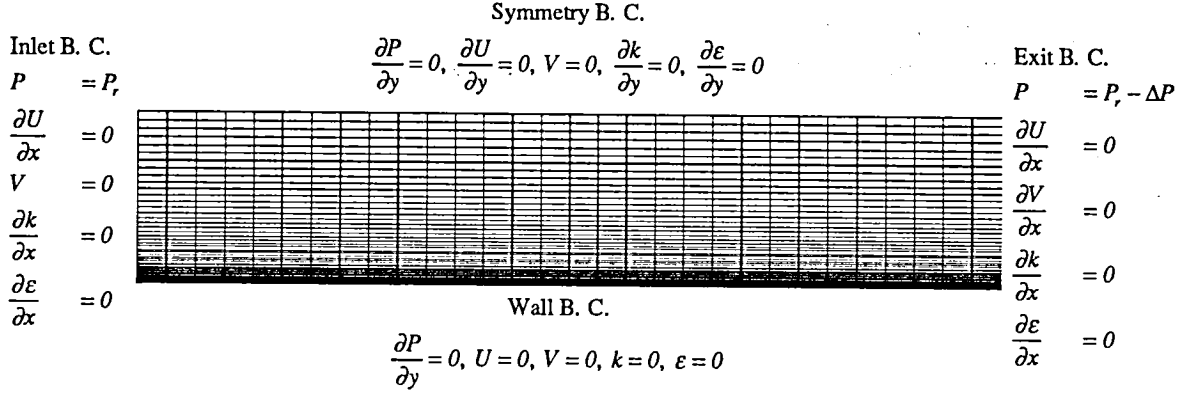


Fig. 1a Grid geometry and boundary conditions for fully developed 2-D channel flow

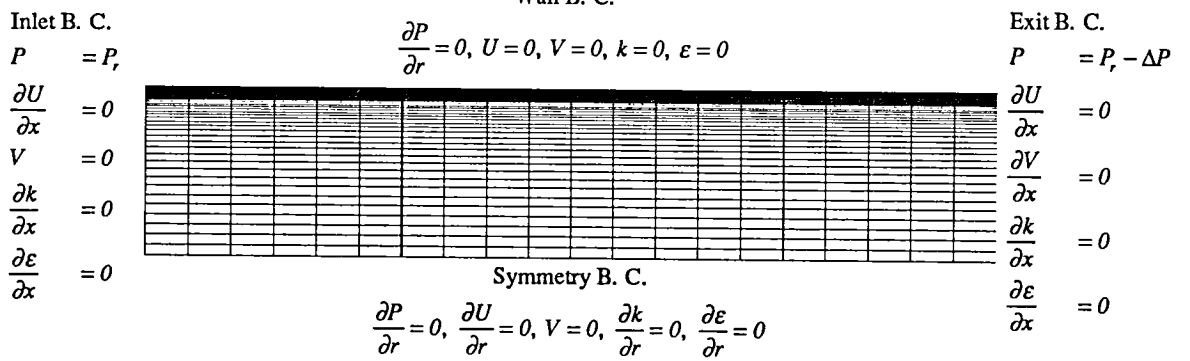


Fig. 1b Grid geometry and boundary conditions for fully developed axisymmetric pipe flow

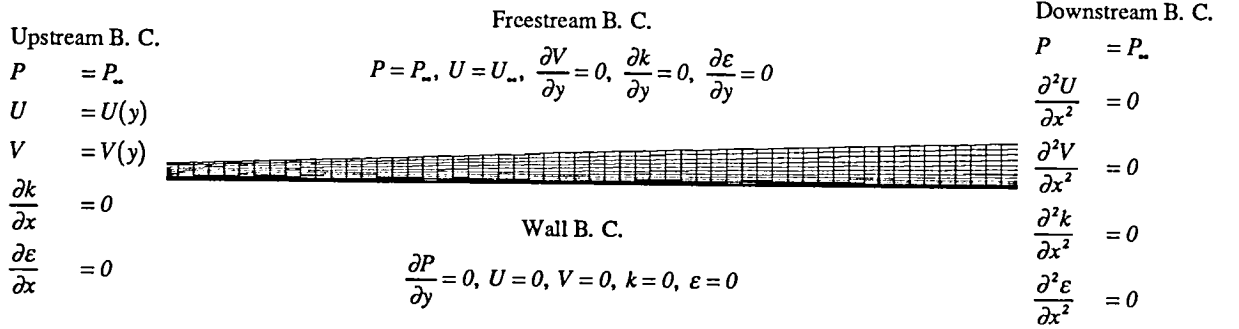


Fig. 1c Grid geometry and boundary conditions for boundary layer flow over a flat plate

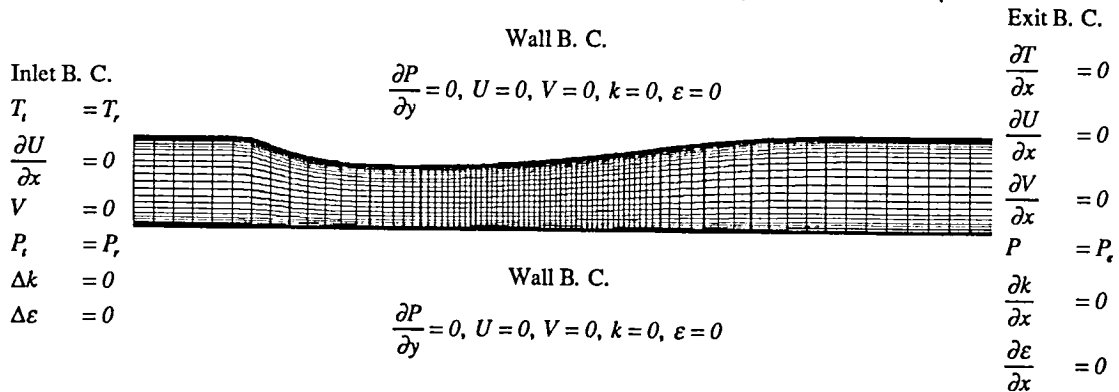


Fig. 1d Grid geometry and boundary conditions for Sajben diffuser flow



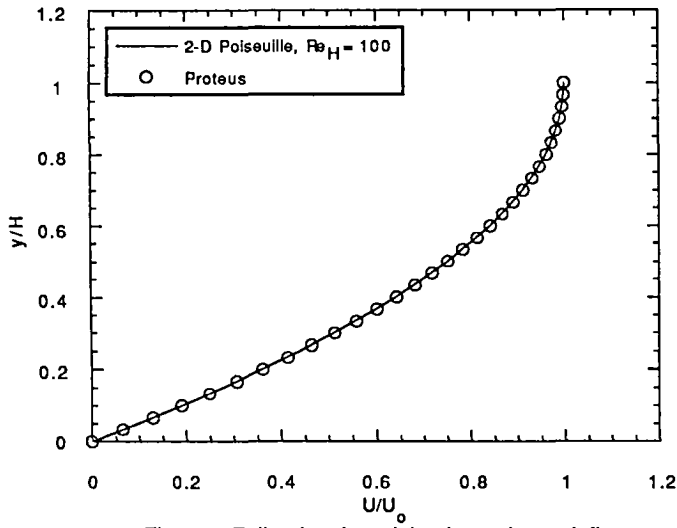


Fig. 2a Fully developed laminar channel flow velocity profile

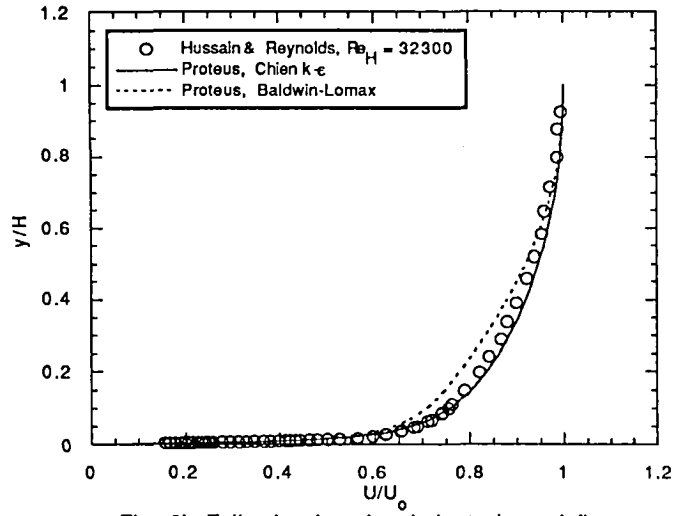


Fig. 2b Fully developed turbulent channel flow velocity profile

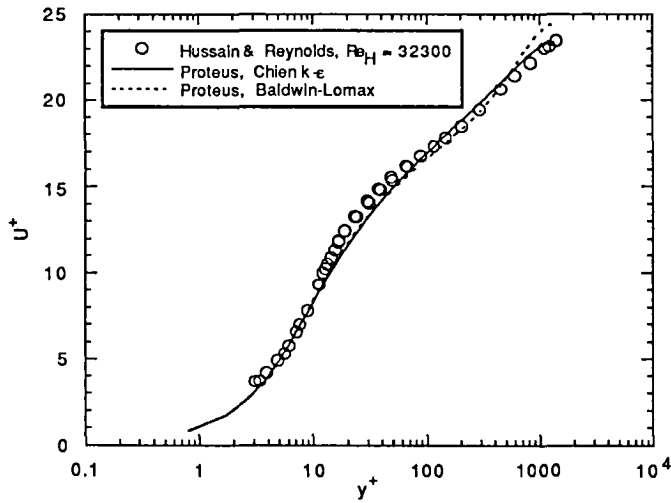


Fig. 2c Fully developed turbulent channel flow  $u^+$  profile

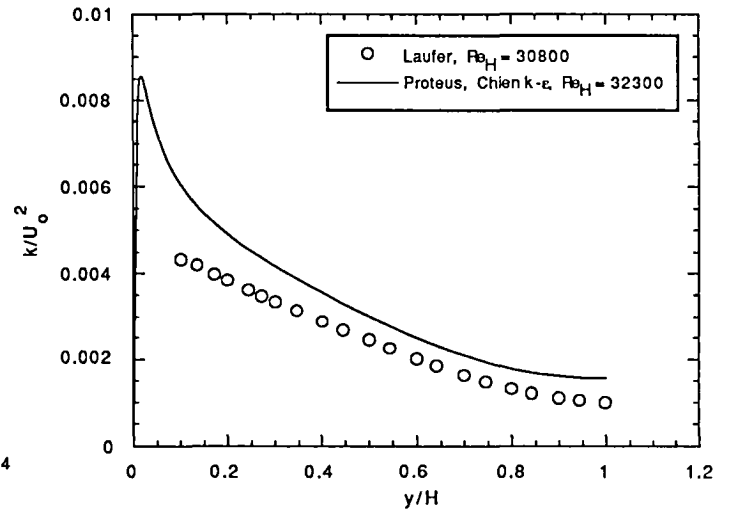


Fig. 2d Fully developed turbulent channel flow kinetic energy profile

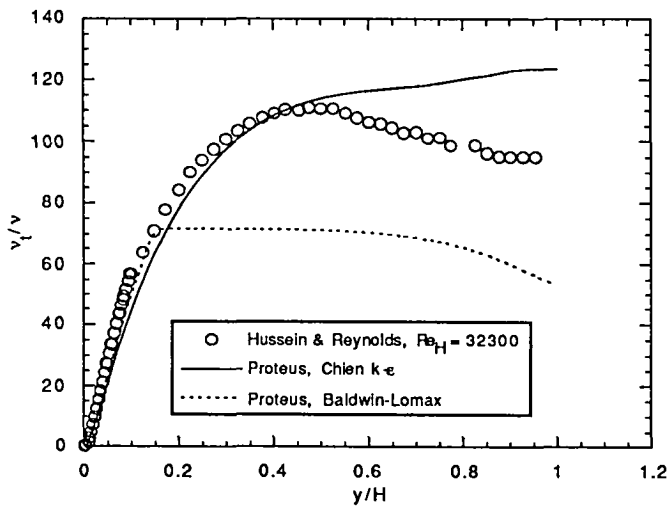


Fig. 2e Fully developed turbulent channel flow eddy viscosity profile

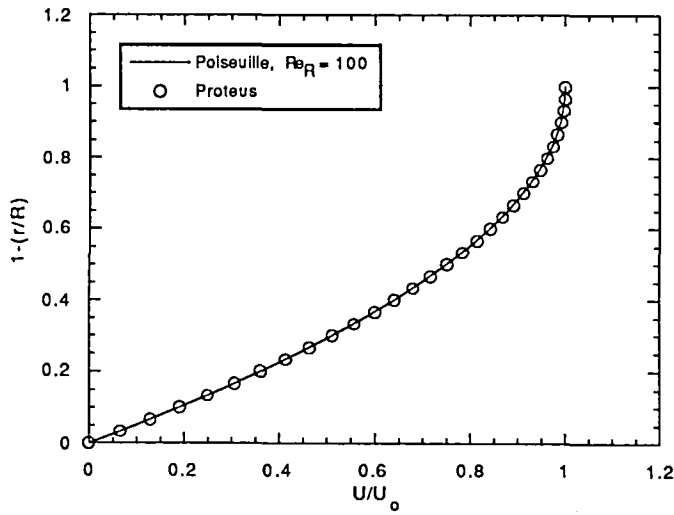


Fig. 3a Fully developed laminar pipe flow velocity profile

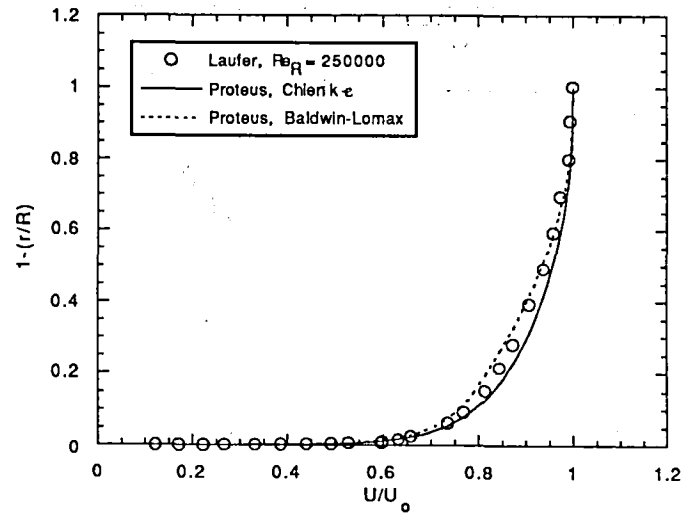


Fig. 3b Fully developed turbulent pipe flow velocity profile

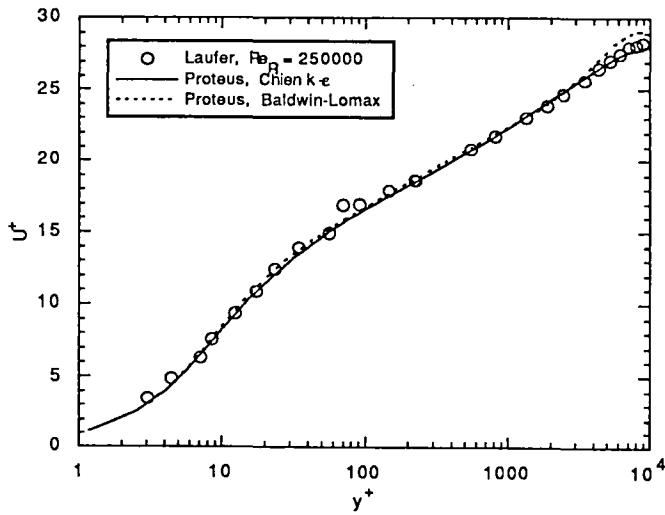


Fig. 3c Fully developed turbulent pipe flow  $u^+$  profile

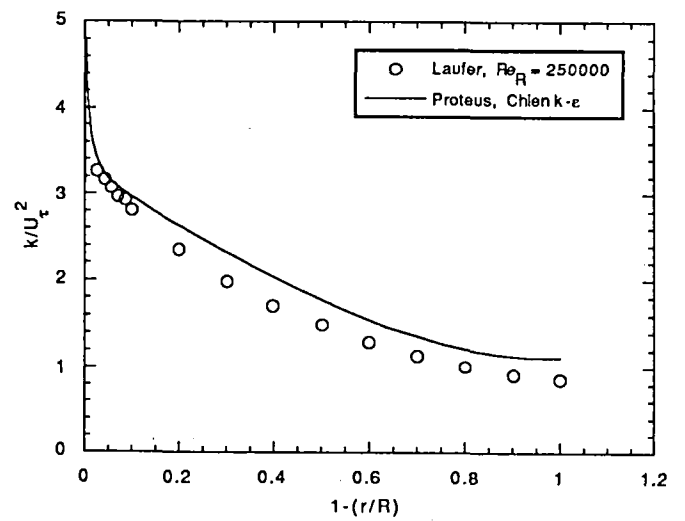


Fig. 3d Fully developed turbulent pipe flow kinetic energy profile

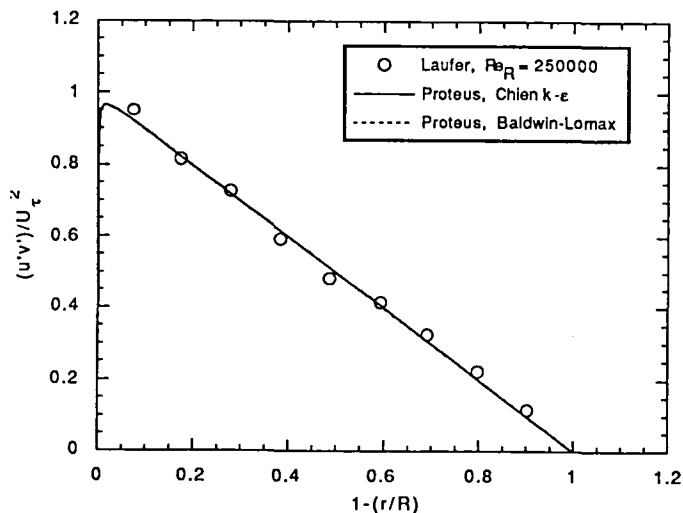


Fig. 3e Fully developed turbulent pipe flow Reynolds stress profile

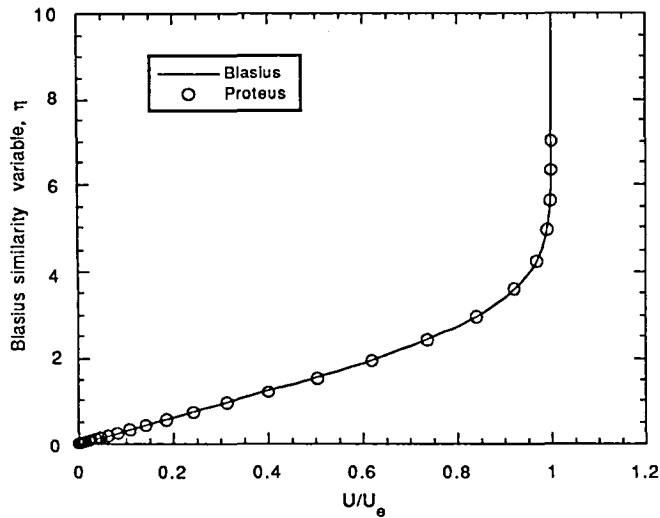


Fig. 4a Laminar boundary layer velocity profile

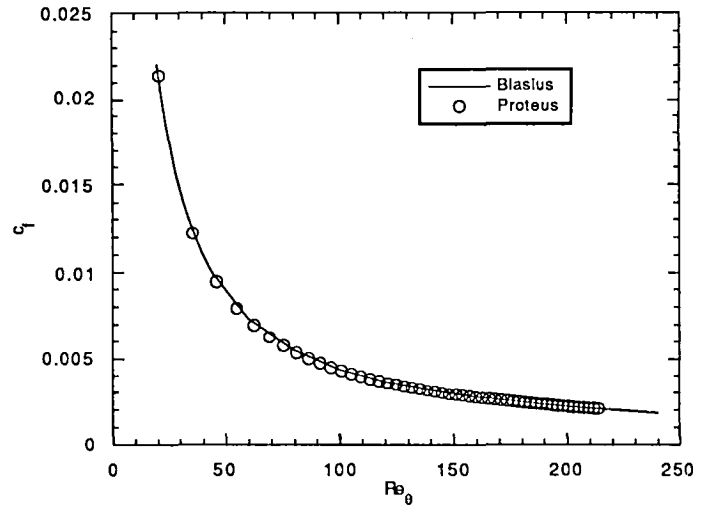


Fig. 4b Laminar boundary layer local skin friction coefficient distribution

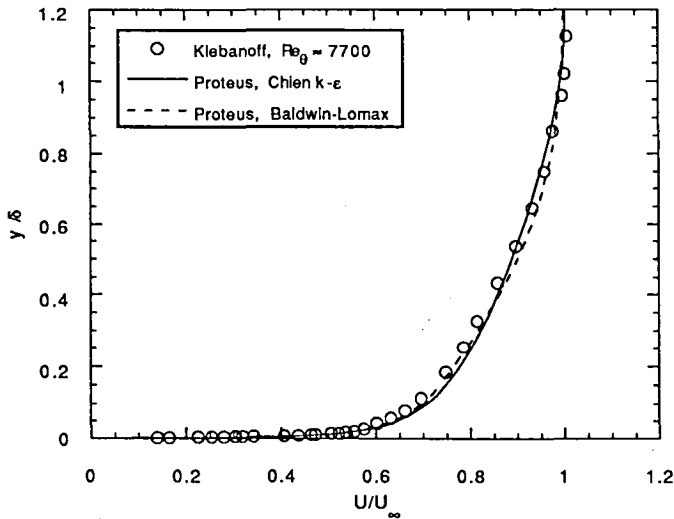


Fig. 4c Turbulent boundary layer velocity profile

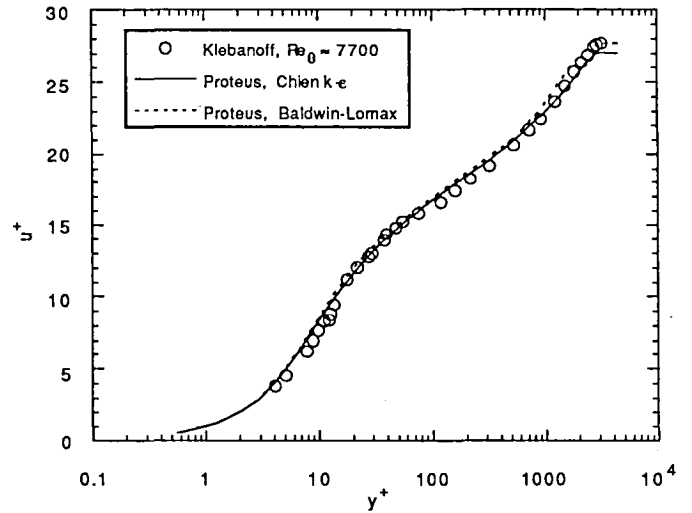


Fig. 4d Turbulent boundary layer  $u^+$  profile

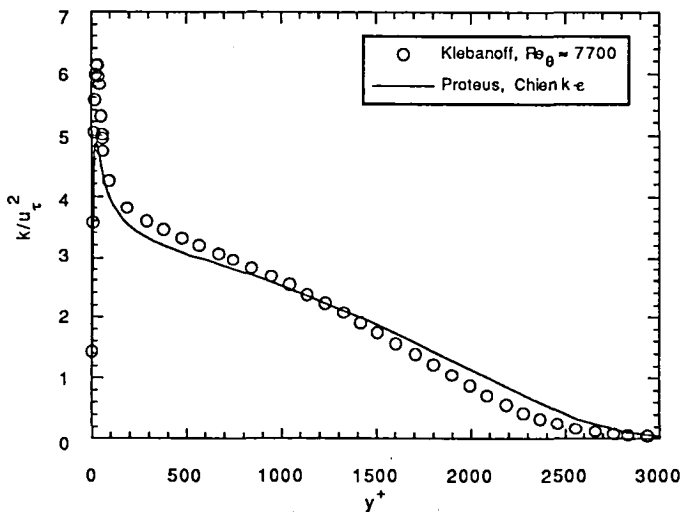


Fig. 4e Turbulent boundary layer kinetic energy profile

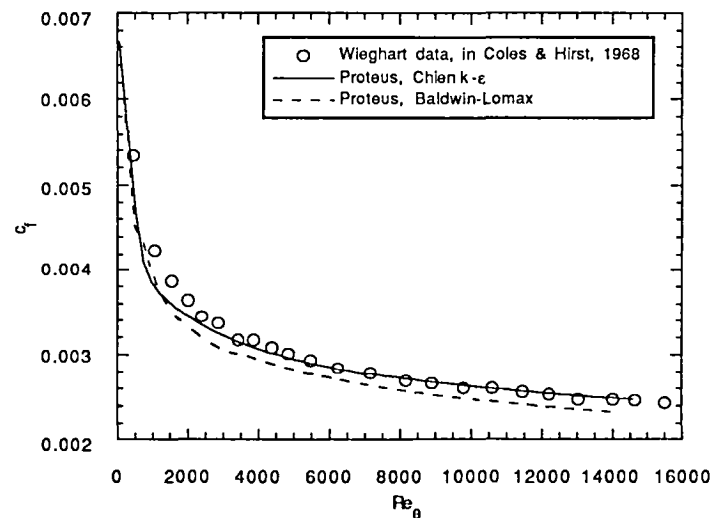


Fig. 4f Turbulent boundary layer local skin friction coefficient distribution

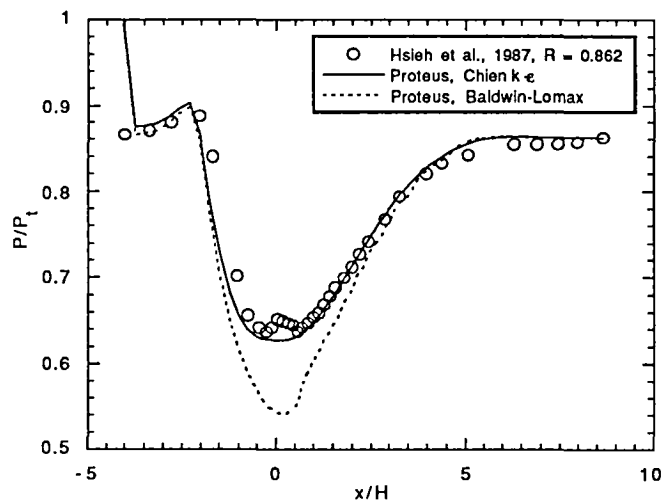


Fig. 5a Sajben diffuser top wall pressure distribution, no shock case

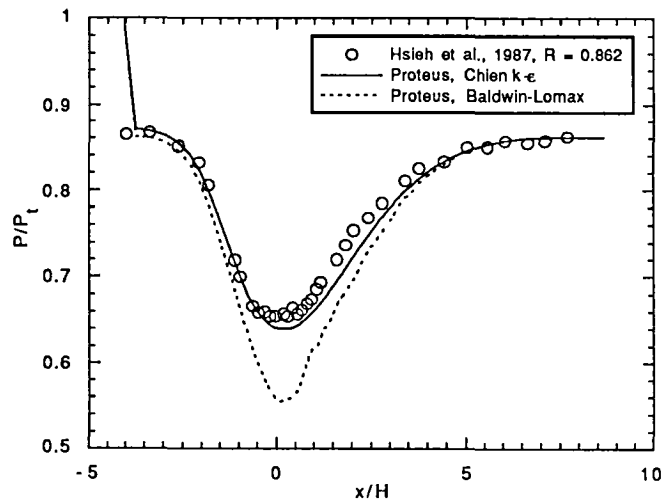


Fig. 5b Sajben diffuser lower wall pressure distribution, no shock case

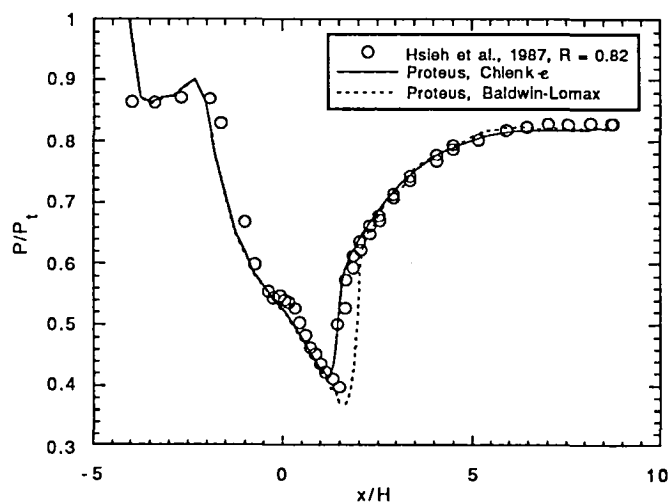


Fig. 5c Sajben diffuser top wall pressure distribution, weak shock case

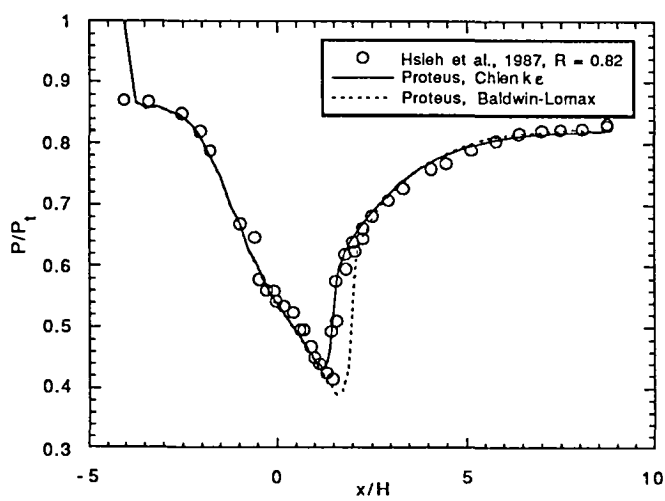


Fig. 5d Sajben diffuser lower wall pressure distribution, weak shock case

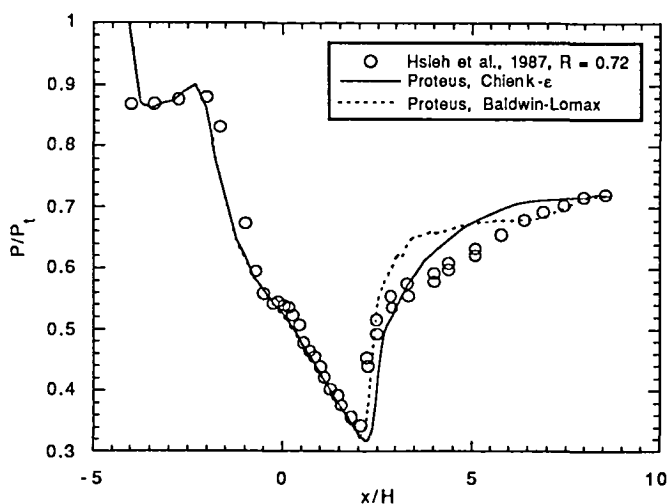


Fig. 5e Sajben diffuser top wall pressure distribution, strong shock case

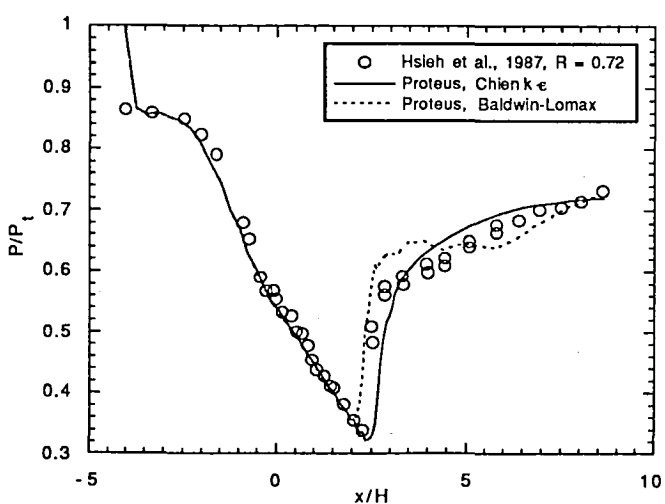
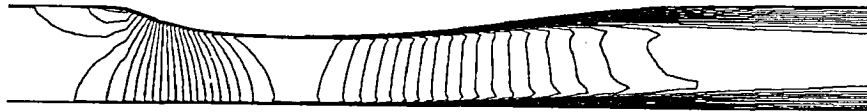
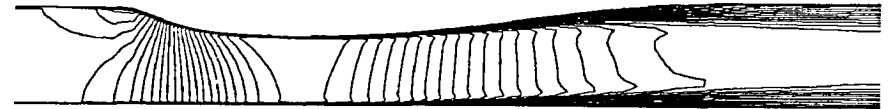


Fig. 5f Sajben diffuser lower wall pressure distribution, strong shock case



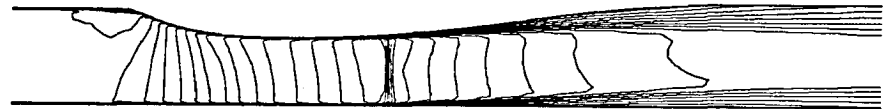
a. Baldwin-Lomax model,  $R = 0.862$ ,  $M_{\max} = 0.98$



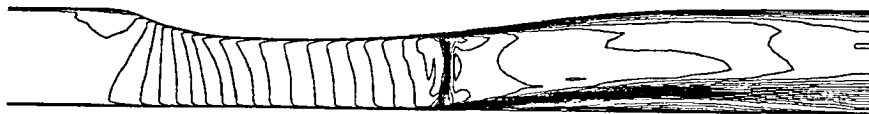
b. Chien  $k-\epsilon$  model,  $R = 0.862$ ,  $M_{\max} = 0.84$



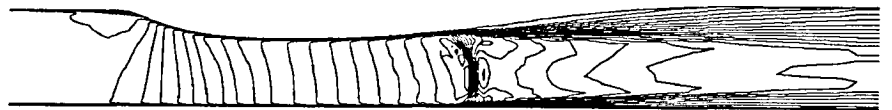
c. Baldwin-Lomax model,  $R = 0.82$ ,  $M_{\max} = 1.34$



d. Chien  $k-\epsilon$  model,  $R = 0.82$ ,  $M_{\max} = 1.23$



e. Baldwin-Lomax model,  $R = 0.72$ ,  $M_{\max} = 1.44$



f. Chien  $k-\epsilon$  model,  $R = 0.72$ ,  $M_{\max} = 1.50$

Fig. 6 Computed Mach number contours for the Sajben diffuser

REPORT DOCUMENTATION PAGE			Form Approved OMB No. 0704-0188	
Public reporting burden for this collection of information is estimated to average 1 hour per response, including the time for reviewing instructions, searching existing data sources, gathering and maintaining the data needed, and completing and reviewing the collection of information. Send comments regarding this burden estimate or any other aspect of this collection of information, including suggestions for reducing this burden, to Washington Headquarters Services, Directorate for Information Operations and Reports, 1215 Jefferson Davis Highway, Suite 1204, Arlington, VA 22202-4302, and to the Office of Management and Budget, Paperwork Reduction Project (0704-0188), Washington, DC 20503.				
1. AGENCY USE ONLY (Leave blank)		2. REPORT DATE April 1992		3. REPORT TYPE AND DATES COVERED Technical Memorandum
4. TITLE AND SUBTITLE Implementation/Validation of a Low Reynolds Number Two-Equation Turbulence Model in the Proteus Navier-Stokes Code – Two-Dimensional/Axisymmetric			5. FUNDING NUMBERS  WU-505-62-52	
6. AUTHOR(S) Trong T. Bui				
7. PERFORMING ORGANIZATION NAME(S) AND ADDRESS(ES)  National Aeronautics and Space Administration Lewis Research Center Cleveland, Ohio 44135-3191			8. PERFORMING ORGANIZATION REPORT NUMBER  E-6955	
9. SPONSORING/MONITORING AGENCY NAMES(S) AND ADDRESS(ES)  National Aeronautics and Space Administration Washington, D.C. 20546-0001			10. SPONSORING/MONITORING AGENCY REPORT NUMBER  NASA TM-105619	
11. SUPPLEMENTARY NOTES Responsible person, Trong T. Bui, (216) 433-5639.				
12a. DISTRIBUTION/AVAILABILITY STATEMENT  Unclassified - Unlimited Subject Category 34			12b. DISTRIBUTION CODE	
13. ABSTRACT (Maximum 200 words)  The implementation and validation of the Chien low Reynolds number k-ε turbulence model in the two-dimensional/axisymmetric version of Proteus, a compressible Navier-Stokes computer code, are presented. The set of k-ε equations are solved by marching in time using a coupled alternating direction implicit (ADI) solution procedure with generalized first- or second-order time differencing. To validate Proteus and the k-ε turbulence model, laminar and turbulent computations have been done for several benchmark test cases: incompressible fully developed 2-D channel flow, fully developed axisymmetric pipe flow, boundary layer flow over a flat plate, and turbulent Sajben subsonic/transonic diffuser flows. Proteus results from these test cases showed good agreement with analytical results and experimental data. Detailed comparisons of both mean flow and turbulent quantities demonstrated that the Chien k-ε turbulence model gives good results over a wider range of turbulent flows than the Baldwin-Lomax turbulence model in the Proteus code with no significant CPU time penalty for more complicated flow cases.				
14. SUBJECT TERMS Navier-Stokes equation; Turbulence; Alternating Direction Implicit methods			15. NUMBER OF PAGES 20	
			16. PRICE CODE A03	
17. SECURITY CLASSIFICATION OF REPORT Unclassified	18. SECURITY CLASSIFICATION OF THIS PAGE Unclassified	19. SECURITY CLASSIFICATION OF ABSTRACT Unclassified	20. LIMITATION OF ABSTRACT	



National Aeronautics and  
Space Administration

**Lewis Research Center**  
Cleveland, Ohio 44135

Official Business  
Penalty for Private Use \$300

**FOURTH CLASS MAIL**

ADDRESS CORRECTION REQUESTED



Postage and Fees Paid  
National Aeronautics and  
Space Administration  
NASA 451

**NASA**

---